Available online at www.sciencedirect.com
ScienceDirect
Chaos, Solitons and Fractals xxx (2007) xxx–xxx
CHAOS SOLITONS & FRACTALS
www.elsevier.com/locate/chaos

Spurious structures in chaos indicators maps

R. Barrio [a,*,1], W. Borczyk [b], S. Breiter [b,2]

[a] GME, Depto. Matemática Aplicada and IUMA, Universidad de Zaragoza, E-50009 Zaragoza, Spain
[b] Astronomical Observatory of A. Mickiewicz University, Sloneczna 36, PL 60-286 Poznań, Poland

Accepted 13 September 2007

Abstract

The paper confronts chaos indicators of two basic types: spectral methods and variational methods. The spectral methods include the spectral numbers and the integrated autocorrelation function. Variational methods discussed are FLI, MEGNO and OFLI2. Using an ad hoc model of coupled pendulum we demonstrate various spurious patterns that appear in the maps of the chaos indicators. Spectral methods generate spurious Moiré fringes, whereas variational methods are sensitive to the integration time or – in the case of the first-order variations indicators – to the initial direction of the variations vector. An example of major discrepancy between the two kinds of methods is given for an unstable periodic orbit. The influence of the initial variations vector is explained in the context of Lyapunov vectors theory and some selection rules are recommended.

1. Introduction

One of the most important and, why not to say, most popular mathematical theories of the 20th century has been the chaos theory. Therefore, an analysis of the regular and chaotic behavior of a dynamical system has became more and more important. The problem of answering if some given initial conditions generate a chaotic orbit or not, or if a given dynamical system is regular or chaotic is not an easy task. First, we have to answer what we consider a chaotic orbit and a chaotic system. There are dozens of definitions in literature, but without any doubt the most well known mathematical definition of a chaotic system is the Devaney's [1]:

Definition 1. We say that $f: X \to X$ is *chaotic* on X if

(1) f is transitive,
(2) the set of periodic orbits of f is dense in X,
(3) f has sensitive dependence on initial conditions.

* Corresponding author. Tel.: +34 976 762480; fax: +34 976 761140.
E-mail addresses: rbarrio@unizar.es (R. Barrio), bori@moon.astro.amu.edu.pl (W. Borczyk), breiter@amu.edu.pl (S. Breiter).
[1] Supported partially by the Spanish Research Grant MTM2006-06961.
[2] Supported partially by the Spanish Research Grant ESP2005-07107.

0960-0779/$ - see front matter © 2007 Elsevier Ltd. All rights reserved.
doi:10.1016/j.chaos.2007.09.084

Note that recently it has been proved [2] that if the function is continuous, the third condition is implied by the first two and therefore, it is redundant. On the other hand, the chaos definition in applied sciences is actually based upon the third postulate.

Once the definition of chaos has been established, we may study the chaoticity of a system; but doing it in rigorously is not easy and moreover, it is not always possible. Therefore, any fast and easy technique that permits us to locate regions where chaos is probable is very useful. Several of such techniques (chaos indicators) have appeared during the last few years, but most of them may give us wrong results or at least create some spurious structures when they are used without care. The main objective of this paper is to study few popular chaos indicators, to confront their results in order to identify spurious patterns in chaoticity maps, to explain their origin and to hint how to avoid them. We also propose a new spectral type indicator and a Hamiltonian test system with two degrees of freedom that has some interesting properties.

The paper is organized as follows: Section 2 describes some chaos indicators, in Section 3 we presents the tests problems and in Section 4 we analyze the results.

2. Selected methods

In this paper, we focus our attention on two types of chaos indicators: variational and spectral methods. In the literature there exist a vast number of these kinds of indicators and of other kinds not studied here, some of them designed for maps (for example, see [3–8]).

2.1. Variational methods

Variational methods explore the behavior of variations vector $\boldsymbol{\xi}$ associated with a given fiducial trajectory $\boldsymbol{\rho}(t)$. Alternatively, we will also use the symbol $\delta\boldsymbol{\rho} \equiv \boldsymbol{\xi}$. For a dynamical system with continuous time t

$$\dot{\boldsymbol{\rho}} = \boldsymbol{f}(t, \boldsymbol{\rho}), \tag{1}$$

the evolution of $\boldsymbol{\xi}$ obeys linear differential equations

$$\dot{\boldsymbol{\xi}} = D\boldsymbol{f}(t, \boldsymbol{\rho}(t))\boldsymbol{\xi}. \tag{2}$$

For discrete maps that generate $\boldsymbol{\rho}_n$ with $n \in \mathbb{N}$, the evolution of $\boldsymbol{\xi}$ is defined as a linear map

$$\boldsymbol{\xi}_n = D\boldsymbol{\rho}_{n-1}\boldsymbol{\xi}_{n-1}. \tag{3}$$

Analyzing the evolution of the norm of $\boldsymbol{\xi}$ provides important information about the properties of motion. If $\xi = \|\boldsymbol{\xi}\|$ grows exponentially, the motion has sensitive dependence on initial conditions and the fiducial orbit $\boldsymbol{\rho}(t)$ is considered chaotic, provided $\rho(t)$ is bounded [9]. The sensitivity is reflected in the positive value of the maximum Lyapunov characteristic exponent (MLCE) λ [10,11]. However, one should bear in mind an important clause concerning a chaotic orbit: not only it has to be bounded and posses a positive MLCE, but also it cannot be asymptotically periodic/quasi-periodic [12].

Out of the plethora of variational methods we have selected three: the MEGNO of Cincotta and Simó [13], FLI [14,15] and OFLI2 of Barrio [16,17].

2.1.1. MEGNO

The Mean Exponential Growth factor of Nearby Orbits (MEGNO) is a linear variational method introduced by Cincotta and Simó [13,18]. In the present paper we use the discrete time variant of the MEGNO method that can be applied to the sequence $\boldsymbol{\rho}_i = \boldsymbol{\rho}(t_0 + ih)$, where $0 \leqslant i \leqslant N$. The MEGNO indicator in this case is defined as [18]

$$\overline{Y}(N) = \frac{1}{N}\sum_{k=1}^{N} Y(k), \tag{4}$$

where

$$Y(k) = \frac{1}{k}\sum_{j=1}^{k} j \ln\frac{\|\boldsymbol{\xi}_j\|}{\|\boldsymbol{\xi}_{j-1}\|}. \tag{5}$$

Please cite this article in press as: Barrio R et al., Spurious structures in chaos indicators maps, Chaos, Solitons & Fractals (2007), doi:10.1016/j.chaos.2007.09.084

Instead of using the direct definition (4) it can be more advantageous to evaluate the running average

$$Y_n = \frac{n-1}{n} Y_{n-1} + 2\ln\left(\frac{\|\xi_n\|}{\|\xi_{n-1}\|}\right), \tag{6}$$

$$\overline{Y}_n = \frac{1}{n}[(n-1)\overline{Y}_{n-1} + Y_n] \tag{7}$$

like in [19].

The properties of MEGNO make it one of the best variational methods. The values of $\overline{Y}$ provide the "absolute" information because for a chaotic orbit $\overline{Y}$ grows linearly with time and $\mathrm{d}\overline{Y}/\mathrm{d}t$ asymptotically tends to $\lambda/2$ allowing an accurate determination of MLCE. Ordered motion results asymptotically in $\overline{Y} = 2$, with the exception of harmonic oscillations where $\overline{Y}$ tends to 0. Thus the values of MEGNO lower than 2 usually indicate the neighborhood of a stable equilibrium. Many applications [19–24] confirmed that MEGNO is an efficient and reliable indicator.

2.1.2. FLI and OFLI2

The Fast Lyapunov Indicator (FLI) was introduced by Froeschlé and Lega [15]; it is defined as the initial part (up to a stopping time t_f) of the computation of the MLCE:

$$\mathrm{FLI}(\boldsymbol{\rho}(0), \boldsymbol{\xi}(0), t_f) = \sup_{0<t<t_f} \ln\|\boldsymbol{\xi}(t)\|.$$

A modified variant known as OFLI (Orthogonal Fast Lyapunov Indicator) was introduced in [14], intended to facilitate the detection of periodic orbits. Similarly to the FLI, it is defined as

$$\mathrm{OFLI}(\boldsymbol{\rho}(0), \boldsymbol{\xi}(0), t_f) = \sup_{0<t<t_f} \ln\|\boldsymbol{\xi}^{\perp}(t)\|,$$

but here $\boldsymbol{\xi}^{\perp}$ is the component of $\boldsymbol{\xi}$ orthogonal to the flow at the point $\boldsymbol{\rho}$. The OFLI tends to a constant value for the periodic orbits, behaves linearly for initial conditions on a KAM torus and on a regular resonant motion (but with different rate growth rate) and grows exponentially for chaotic orbits. This indicator is one of the fastest chaos indicators used in the literature.

The FLI indicator (as well as the OFLI) suffers from several disadvantages; one of them is its dependence on the choice of initial conditions $\boldsymbol{\xi}(0)$ for the variational equations. The $\mathrm{OFLI}^2_{\mathrm{TT}}$ indicator was proposed by Barrio [16] as a way to resolve this problem. In order to cut short the grandiloquent acronym, we will use a simpler abbreviation OFLI2, meaning at the final time t_f

$$\mathrm{OFLI2} \equiv \mathrm{OFLI}^2_{\mathrm{TT}} := \sup_{0<t<t_f} \ln\left\|\left\{\boldsymbol{\xi}(t) + \frac{1}{2}\delta\boldsymbol{\xi}(t)\right\}^{\perp}\right\|, \tag{8}$$

where $\boldsymbol{\xi}$ and $\delta\boldsymbol{\xi}$ are the first and second-order sensitivities with respect to carefully chosen initial vectors. In this case the variational equations up to second-order and the initial conditions are

$$\begin{aligned}
&\frac{\mathrm{d}\boldsymbol{\rho}}{\mathrm{d}t} = \boldsymbol{f}(t,\boldsymbol{\rho}), \quad \boldsymbol{\rho}(0) = \boldsymbol{\rho}_0,\\
&\frac{\mathrm{d}\boldsymbol{\xi}}{\mathrm{d}t} = \frac{\partial \boldsymbol{f}(t,\boldsymbol{\rho})}{\partial \boldsymbol{\rho}}\boldsymbol{\xi}, \quad \boldsymbol{\xi}(0) = \frac{\boldsymbol{f}(0,\boldsymbol{\rho}_0)}{\|\boldsymbol{f}(0,\boldsymbol{\rho}_0)\|},\\
&\frac{\mathrm{d}\delta\xi_j}{\mathrm{d}t} = \frac{\partial f_j}{\partial \boldsymbol{\rho}}\delta\boldsymbol{\xi} + \boldsymbol{\xi}^{\top}\frac{\partial^2 f_j}{\partial \boldsymbol{\rho}^2}\boldsymbol{\xi}, \quad \delta\boldsymbol{\xi}(0) = \mathbf{0}.
\end{aligned} \tag{9}$$

Note that the last line of Eq. (9) is written for a single jth component $\delta\xi_j$ to simplify the notation. The OFLI2 indicator has shown its robustness in several classical problems [17,25].

In contrast to the MEGNO, the methods belonging to the FLI family provide only relative results; one has to apply them to a certain number of orbits including at least one known to be regular and serving as a calibration benchmark.

2.2. Spectral methods

Typical spectral methods focus on a single orbit, paying no attention to its neighborhood in the phase space. This point makes them essentially different from variational methods. Analyzing the spectrum of some scalar function $q(\boldsymbol{\rho}(t))$ that maps $\boldsymbol{\rho}$ on a bounded subset of real numbers, or rather the discrete argument time series

$$q = \{q_i : q_i = q(\boldsymbol{\rho}(t_0 + ih)), 0 \leqslant i \leqslant N\}, \tag{10}$$

Please cite this article in press as: Barrio R et al., Spurious structures in chaos indicators maps, Chaos, Solitons & Fractals (2007), doi:10.1016/j.chaos.2007.09.084

one tries to decide if the power spectrum of q is discrete or continuous. In a more sophisticated approach proposed by Laskar [26,27], the dependence of the leading frequency peaks on the time interval, initial conditions or parameters is studied, but in the present paper we focus only on more straightforward methods. We are going to confront variational methods with simple counting of the frequency peaks (spectral number) and with the integrated autocorrelation function. According to the Wiener–Khinchin theorem, autocorrelation carries the same information as the Fourier transform of q. This is why we qualify an autocorrelation-based detector as a spectral method.

2.2.1. Spectral number (SN)

Probably the most simple of spectral methods consists in counting the number of peaks in the power spectrum of some function $q(\boldsymbol{\rho}(t))$ [28]. The power spectrum can be best evaluated using the FFT algorithm applied to time series (10). A tricky point in this method is to select an appropriate level of noise A^* and to count only the peaks that are higher than this level. A sine wave with sufficiently large amplitude and zero average should result in a single amplitude and then the amplitude number is SN = 1. The more complicated is motion, the more amplitudes are detected and their number SN considerably grows. This tool has a reputation of being very sensitive, but – similarly to the FLI family – it only detects relative patterns and a distinction between the chaotic and quasi-periodic motion involves some heuristic judgement.

In this paper, we use the implementation of the FFT algorithm from *Numerical Recipes* [29].

2.2.2. Integrated autocorrelation function (IAF)

Given an evenly spaced time series (10) one defines the autocorrelation function estimator C_j

$$C_j = \frac{\sum_{i=0}^{N-j}(q_i - \bar{q})(q_{i+j} - \bar{q})}{\sum_{i=0}^{N-j}(q_i - \bar{q})^2}, \tag{11}$$

where $\bar{q} = (N+1)^{-1}\sum_{i=0}^{N} q_i$ is the mean value estimator [30]. Recalling the fact that only a finite number of points q_i is available, one should not use too large lags j, because then the covariance in the numerator, and variance in the denominator of Eq. (11) might be poorly estimated. Usual rules of thumb restrict the use of Eq. (11) to $j \leqslant N/2$ or even $j \leqslant N/4$. However, if the estimator (11) is replaced by the Pearson product-moment estimator [31]

$$C_j = \frac{\sum_{i=0}^{N-j}(q_i - \bar{q}_i)(q_{i+j} - \bar{q}_{i+j})}{\left(\sum_{i=0}^{N-j}(q_i - \bar{q}_i)^2 \sum_{i=0}^{N-j}(q_{i+j} - \bar{q}_{i+j})^2\right)^{1/2}}, \tag{12}$$

where

$$\bar{q}_j = \frac{1}{(j+1)}\sum_{i=0}^{j} q_i \tag{13}$$

is the mean value of a subset of data, then higher values of lags can be considered – up to $j \leqslant 3N/4$ or more.

Autocorrelation function of periodic (or quasi-periodic) time series is an asymptotically periodic (or quasi-periodic) function of lag, oscillating in the $-1 \leqslant C_j \leqslant 1$ range. On the other extreme, white noise is "delta-correlated" i.e. $C_j = \delta_{0j}$ [10]. Deterministic chaos generates time series whose autocorrelation takes form of exponentially damped oscillations. The e-fold decay time of autocorrelation is often proportional to the Lyapunov time and sometimes referred to as the "poor man's Lyapunov time" [30].

Instead of estimating the e-fold decay time, we would like to propose the application of an indicator whose idea goes back to Norbert Wiener. Our indicator $W(K)$ is the inverse of the so called integrated autocorrelation function

$$W(K) = \frac{K+1}{\sum_{j=0}^{K} C_j^2}. \tag{14}$$

Recalling the properties of autocorrelation one should expect that if q is constant time series $(\forall(i,j)\ q_i = q_j)$, then $W = 1$. If q_i are obtained from a sampled sine wave, the value of W asymptotically tends to $W = 2$. Other periodic or quasi-periodic time series should provide W converging to some finite value – typically not far from 2. But if autocorrelation is exponentially damped, W will tend to infinity and its growth rate should be inversely proportional to the "poor man's Lyapunov time". In this respect the W function behaves similarly to MEGNO and shares its advantage of absolute scaling. In particular, the white noise time series lead to $W(K) = K$ and so we obtain the natural bounds

$$1 \leqslant W(K) \leqslant K,$$

that hold for a sufficiently large maximum lag K.

Please cite this article in press as: Barrio R et al., Spurious structures in chaos indicators maps, Chaos, Solitons & Fractals (2007), doi:10.1016/j.chaos.2007.09.084

Direct computation of W is a costly procedure of the $O(N \times K)$ type. One way to reduce the cost is to use the FFT and reconstruct W from the power spectrum. The method is quick, but limited to the original definition (11), hence only the small lags are reliably accounted for. However, we have tested a simpler approach based on the idea of logarithmic lags cascades, originally invented as a remedy for hardware limitations in the photon counting experiments. In [32], an integer "base number" $B \in \mathbb{N}$ is introduced, generating the sequence of almost logarithmically spaced, integer lags

$$J_0 = 0, \quad J_1 = 1, \quad J_k = J_{k-1} + 2^{[(k-1)/B]}, \tag{15}$$

where $[x]$ stands for the integer part of x. In the limit case $B \geqslant K$, autocorrelation values for all lags $0 \leqslant j \leqslant K$ are taken into account in Eq. (14). Smaller base numbers result in selecting only a subset of lags to compute W: first $B+1$ lags $J_0, \ldots, J_B$ are equally spaced with $J_k - J_{k-1} = 1$, next B lags have the spacing 2, next B differ by 4, then by 8 and so on. In particular, $B = 1$ results in an extremely sparse set of lags $\{0, 1, 2, 4, 8, 16, 32, \ldots\}$. In our application, it is more appropriate to sample large lags more densely than the small ones. So we invert the lags cascades and use

$$j_k = J_{k^*} - J_{k^*-k}, \tag{16}$$

where k^* is the last index used to generate sample points according to Eq. (15).

Using the almost logarithmic lags and treating the denominator of Eq. (14) as a forward open quadratures formula, we can replace Eq. (14) by

$$W(j_{k^*+1}) = \frac{j_{k^*}}{1 + \sum_{k=1}^{k^*} (j_k - j_{k-1}) C_{j_k}^2}. \tag{17}$$

Thanks to the use of logarithmic lags, the computational cost of IACF is reduced to $O(N \times B \log_2(1 + K/B))$.

3. Test problems

The four methods presented in the previous section will be applied to a simple but instructive test problem: a coupled pendulum system with two degrees of freedom. Introducing two coordinates x, y and their conjugate momenta X, Y we propose the Hamiltonian function

$$\mathscr{H} = \frac{1}{2}(X^2 + Y^2) - (1 + ab)\cos x - a \cos y + ab \cos x \cos y. \tag{18}$$

The Hamiltonian depends on the state variables $\boldsymbol{\rho} = (x, y, X, Y)^\top$ and on two constant real parameters a, b, leading to equations of motion

$$\dot{\boldsymbol{\rho}} = \boldsymbol{f}(\boldsymbol{\rho}) = \begin{pmatrix} X \\ Y \\ -(1 + ab - ab\cos y)\sin x \\ -a(1 - b\cos x)\sin y \end{pmatrix}. \tag{19}$$

The problem is integrable for all initial conditions when either a or b are equal 0. Moreover, for all parameters values it admits four special solutions: $(x = X = 0)$, $(x = \pi, X = 0)$, $(y = Y = 0)$, and $(y = \pi, Y = 0)$, resulting in a simple pendulum motion for the remaining degree of freedom.

Equations of motion (19) are integrated either by means of the Taylor series method [33,34] for the FLI and OFLI2 evaluation, or using the fourth-order symplectic method [35] based on a composition of leapfrogs.

Apart from this new exemplary problem, we also provide some tests on the very classical Hénon–Heiles Hamiltonian [36] given by the Hamiltonian

$$\mathscr{H}(x, y, X, Y) = \frac{1}{2}(X^2 + Y^2 + x^2 + y^2) + x^2 y - \frac{1}{3}y^3. \tag{20}$$

The reason of using this problem is understandable: it was extensively used as a benchmark for chaos indicators (moreover, some methods have been tested only on this problem).

4. Testing the $y = Y = 0$ case of the coupled pendulum

Let us focus on the $y = Y = 0$ case of our double pendulum problem, when

Please cite this article in press as: Barrio R et al., Spurious structures in chaos indicators maps, Chaos, Solitons & Fractals (2007), doi:10.1016/j.chaos.2007.09.084

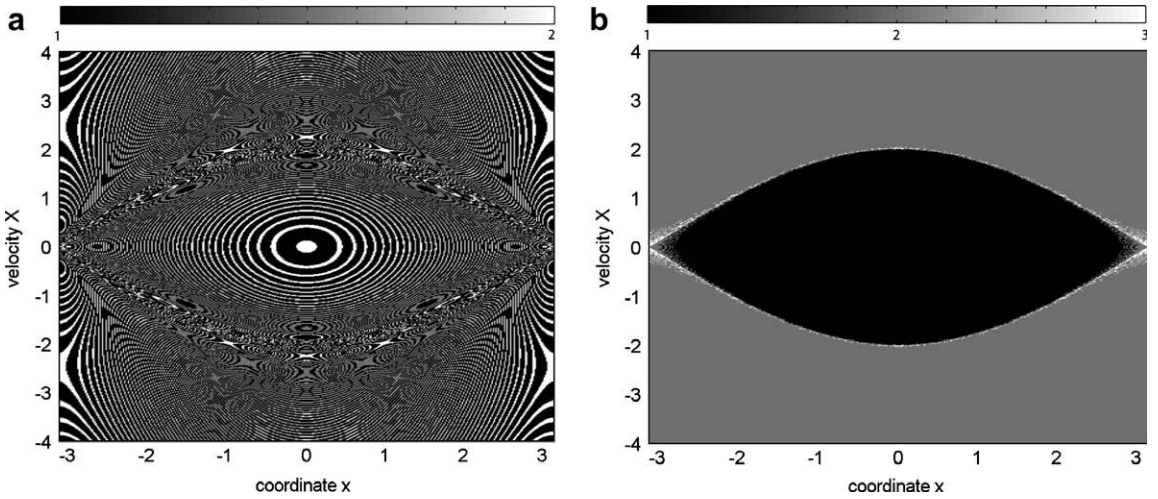

Fig. 1. Simplistic spectral number SSN (a) and spectral number SN (b) for the planar case of the coupled pendulum.

$$\dot{\boldsymbol{\rho}} = (X, 0, -\sin x, 0)^{\top}. \tag{21}$$

Note that this case is the classical planar mathematical pendulum, integrable in terms of elliptic functions. No chaos appears in this problem (unless introduced by a numerical integration method) and all orbits are periodic (non-isochronous) except for the separatrix motion that is asymptotically periodic. The chaos indicators should only detect the vicinity of separatrices as a more complicated periodic motion zone and the vicinity of the stable equilibrium as the region of almost isochronous periodic motion.

Unless otherwise stated, we have fixed the parameter values $a = 4$ and $b = 1$ in all the tests. For all the B&W or color pictures the black or blue color is associated with regular motion and white or red with less regular or chaotic[3].

4.1. Regular or chaotic?

4.1.1. Spectral methods results

Figs. 1 and 2 present the maps of the two spectral chaos indicators. The gray scale of some the figures have been adjusted in order to show more clear the spurious structures, but the global result, all the orbits are regular, is correct. The complete equations of motion (19) were integrated by means of the S_4 method, assuming initial conditions $y(0) = Y(0) = 0$ and different initial values of x and X. In our spectral methods tests we used $q_i = X(t_0 + ih)$, where h is the integration step.

Spectral numbers were evaluated from 2^{15} output points, i.e. the integration interval was $t_f \approx 524$ with the integration step $h = 0.016$. Assuming the cutoff level for the amplitudes $A^* = 0.3 \max A_i$, we first evaluated a "simplistic spectral number" (SSN) counting all amplitudes A_i of the power spectrum that exceeded A^*. The result, resembling the "Opt Art" of Bridget Riley, is shown in Fig. 1a. The visible spurious patterns, that might serve as yet another illustration in *The Theory of the Moiré Phenomenon* [37], are typical (albeit exaggerated here) for the spectral type methods. The Moiré is generated by the spectral leakage phenomenon inherent in discrete Fourier transform methods. Roughly speaking, a pure sine wave with a frequency ω will produce a single amplitude in the power spectrum only in the case when the sampling step h is an integer fraction of the period $2\pi/\omega$. If this is not the case, some fraction of the signal power "leaks" into neighboring frequencies amplitudes, thus increasing the width of a spectral line. Recalling that the integration step in our example is $h = \frac{2}{125}$, we can identify the SSN = 1 stripes in Fig. 1a as the orbits with a fundamental frequency $\omega \approx 125\pi k^{-1}$, where $k \in \mathbb{N}$. But there is also a second reason for the spectral leakage: even if the sampling is performed with a perfect step, the time interval has to cover an integer number of periods in order to obtain a single amplitude in the power spectrum of the sine wave; so even the same orbit may reveal different leakage depending on the initial point for the sampling. The interplay of these two factors results in a fancy but complicated Moiré pattern in Fig. 1a: the values of SSN greater than 1 result from counting the nearby amplitudes that have been amplified due

[3] For interpretation of color in Figs. 4, 6–8 and 10, the reader is referred to the web version of this article.

Please cite this article in press as: Barrio R et al., Spurious structures in chaos indicators maps, Chaos, Solitons & Fractals (2007), doi:10.1016/j.chaos.2007.09.084

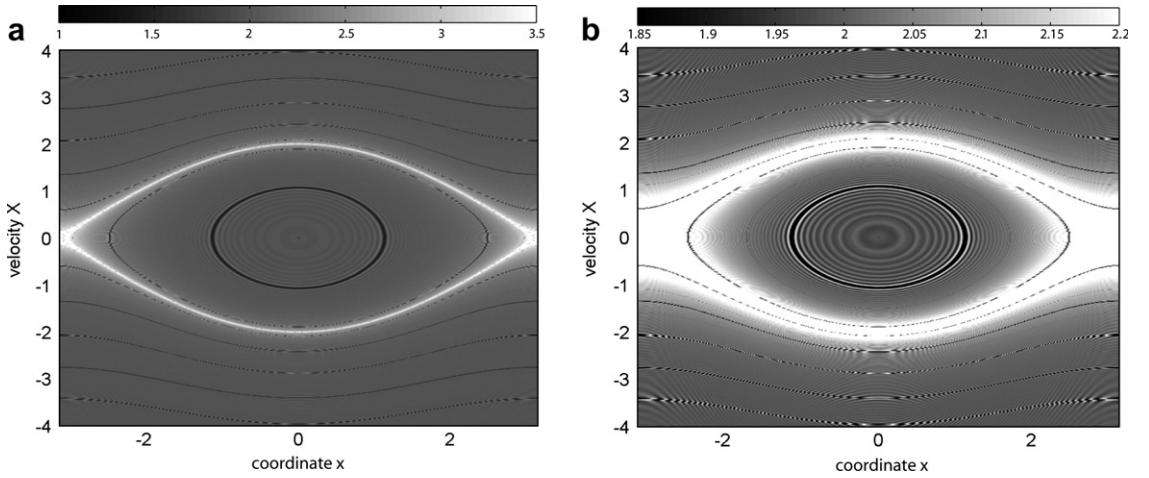

Fig. 2. IACF indicator W for the planar case of the coupled pendulum using two ranges of shades: (a) a typical one and (b) a restricted range to enhance the ripples.

to the spectral leakage. Increasing the sampling rate to tackle the problem is often a costly solution. Using an appropriate window is probably the most elegant solution, but we propose a simpler remedy. Let us count only the peaks of the power spectrum understood as the points A_i where $A_{i-1} - A_i < 0$ and $A_{i+1} - A_i < 0$. For the first and the last amplitude the conditions are $A_1 - A_0 < 0$ for A_0, and $A_N - A_{N-1} > 0$ for A_N. Proceeding this way we obtain the spectral number SN liberated from the problem of counting the same, broad spectrum line more than one time. Fig. 1b provides the SN map obtained with the same sampling rate and time interval. Although it was obtained with a smaller cutoff level $A^* = 0.1 \max A_i$, the results are significantly less noisy and the Moiré has disappeared. We can also well distinguish the libration zone from the circulation domain, owing to the fact that the latter has a significant A_0 coefficient of the constant term (zero frequency). One can see that SSN, as compared to SN, probably deserves a more drastic adjective than "simplistic".

The IACF map was generated using the stepsize $h = 0.02$ and the interval $t_f = 500$. Assuming the base number $B = 40$, we used the maximum lag not exceeding $0.75(t_f/h)$. The map of W values is presented in Fig. 2. Most of the plot is dominated by the $W \approx 2$ shades; the orbits surrounding the separatrix are well visible, with the values of W that typically does not exceed 5 (the exception are two points with $W \approx 9$ at the intersection of the separatrix with $x = 0$). Some orbits reveal the values $W < 2$: two of them are visible inside the libration zone and more in the circulation domain. This is yet another manifestation of the sampling problem and increasing B and/or number and density of output points, one observes that the low W orbits gradually disappear. The Moiré fringes are still present in Fig. 2 although they are more subtle than for the SSN plot; they occur on the level $1.95 < W < 2.05$ at most. Therefore, in Fig. 2a they are almost imperceptible but they appear in Fig. 2b if we use a restricted range of shades to enhance the ripples.

The common conclusion from Figs. 1 and 2 is that from the point of view of spectral indicators, the planar motion of the coupled pendulum is regular and no chaos is visible. Typical spurious features for these methods are the Moiré fringes and "low W" orbits. Both patterns are due to the sampling, that can be reduced by increasing the length and density of the time series considered.

4.1.2. Variational methods results

Knowing the results of spectral indicators, let us now study the planar case of the coupled pendulum ($y = Y = 0$) using the variational methods MEGNO and FLI. Note that we have a choice between two points of view: either we can treat the problem as a pendulum in (x, X) and forget the remaining degree of freedom, or we can only impose the initial conditions $y(0) = Y(0) = 0$ and integrate the complete system with the two degrees of freedom. In the former case only the variations δx and δX can be considered, but in the latter we have to propagate all four components of the variations vector $\boldsymbol{\xi}$, yet still we have a choice between selecting the initial $\delta y = \delta Y = 0$ or letting at least one of them to be nonzero. There is no such freedom (or rather dilemma) neither in the spectral methods (they do not use variations) nor in the OFLI2 (initial variations $\boldsymbol{\xi} = \mathbf{0}$), but for MEGNO and FLI, the choice really matters. Integrating the complete set of Eq. (19) with $\delta y(0) \neq 0$ we obtain the results shown in Fig. 3. Even a quick look brings us to the paradoxical conclusion: the simple pendulum is a chaotic system ! We see the interleaving "chaotic" and "regular" bands in all the

Please cite this article in press as: Barrio R et al., Spurious structures in chaos indicators maps, Chaos, Solitons & Fractals (2007), doi:10.1016/j.chaos.2007.09.084

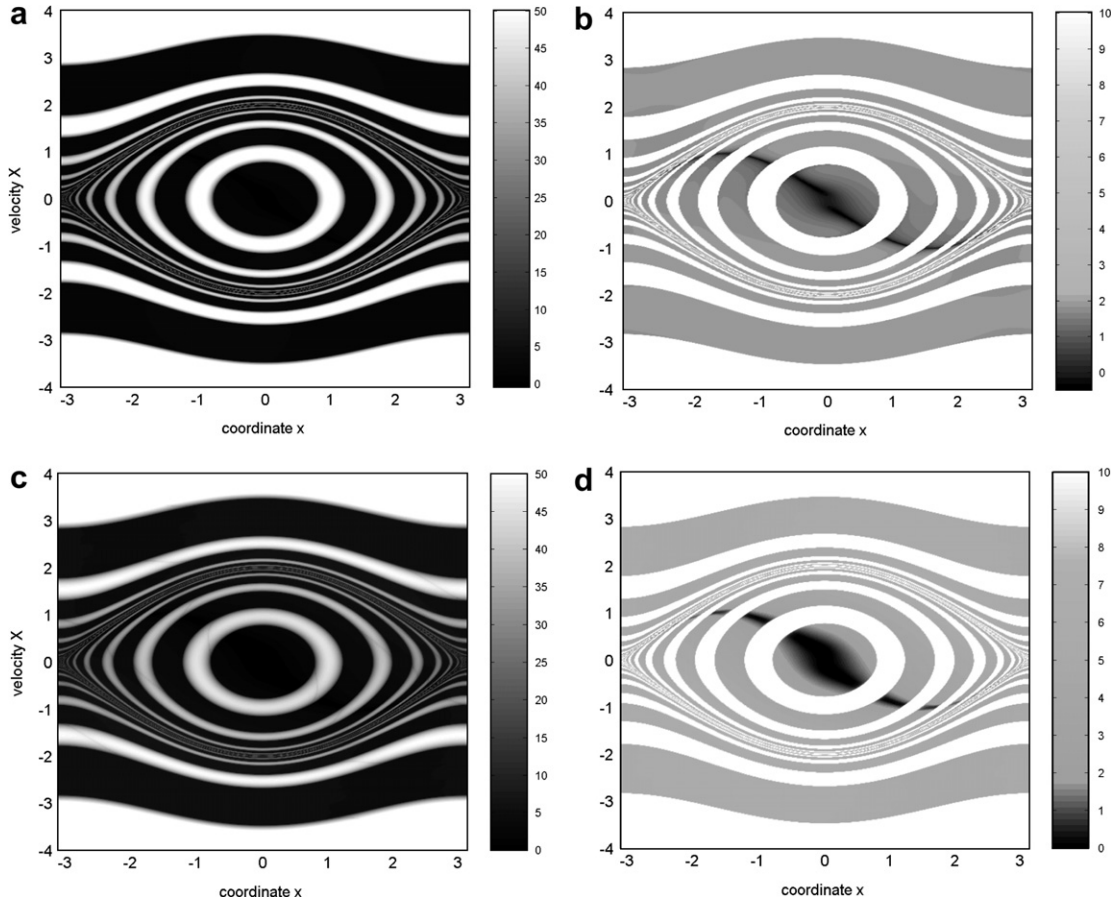

Fig. 3. MEGNO ((a) and (b)) and FLI ((c) and (d)) plots with initial variations $\boldsymbol{\xi}(0) = (1, 1, 1, 0)^{\top}$.

pictures of Fig. 3. But we know well that the system is completely integrable and no chaos has been detected by the spectral methods. So, why the contradiction with spectral methods and the analytical theory?

If we inspect the plots to the right in Fig. 3, based on the same data as the ones to the left but plotted using a truncated scale of shades, we notice another phenomenon: the sine wave of lower MEGNO and FLI values with a bulge at $x = X = 0$. This pattern has to be spurious, because a single libration type orbit intersect it twice and in principle there is no reason to distinguish some initial conditions for a given orbit.

4.1.3. Resolving the contradiction

Can we justify the results of the variational methods from the analytical point of view or shall we blame numerical artifacts? In order to answer this question we have to inspect the variational equations that govern the evolution of $\boldsymbol{\xi}$. Differentiating Eq. (19) we obtain them as

$$\dot{\boldsymbol{\xi}} = \frac{\mathrm{d}}{\mathrm{d}t}\begin{pmatrix} \delta x \\ \delta y \\ \delta X \\ \delta Y \end{pmatrix} = \begin{pmatrix} \delta X \\ \delta Y \\ -\cos x(1 + ab - ab\cos y)\delta x - ab\sin x \sin y\,\delta y \\ -ab\sin x \sin y\,\delta x - a(1 - b\cos x)\cos y\,\delta y \end{pmatrix}. \tag{22}$$

Assuming the planar case $y = Y = 0$ we decouple the variations in both degrees of freedom, because then

$$\dot{\boldsymbol{\xi}} = \frac{\mathrm{d}}{\mathrm{d}t}\begin{pmatrix} \delta x \\ \delta y \\ \delta X \\ \delta Y \end{pmatrix} = \begin{pmatrix} \delta X \\ \delta Y \\ -\cos x\,\delta x \\ -a(1 - b\cos x)\delta y \end{pmatrix} \tag{23}$$

Please cite this article in press as: Barrio R et al., Spurious structures in chaos indicators maps, Chaos, Solitons & Fractals (2007), doi:10.1016/j.chaos.2007.09.084

or simply

$$\delta\ddot{x} = -\cos x\,\delta x, \tag{24}$$

$$\delta\ddot{y} = -a(1 - b\cos x)\delta y. \tag{25}$$

Suppose that we are in the circulation regime and $\cos x \approx \cos vt$. Introducing the new independent variable $u = vt$, and a parameter $\omega^2 = a/v^2$, we can reduce (25) to the standard form of the Mathieu equation

$$\frac{d^2(\delta y)}{du^2} = -\omega^2(1 - b\cos u)\delta y \tag{26}$$

known to be unstable if any of the parametric resonances

$$\omega \approx \frac{k}{2}, \quad k \in \mathbb{Z}_+ \tag{27}$$

occurs [38]. The width of the "Arnold tongues" of instability increases with b but decreases with k. In our case, when $a = 4$, the parametric resonance zones should appear in the neighborhood of

$$v \approx \frac{4}{k}. \tag{28}$$

One can easily verify that subsequent instability stripes in Fig. 3b begin at $X \approx 4$, where $k = 1$, and continue towards the separatrix with $k = 2$, $k = 3$ and so on, becoming thinner and thinner and creating more and more dense pattern. The instability ovals inside the libration zone can also be explained in terms of the Mathieu equation model, but the reduction is more subtle: it requires considering $\cos x \approx 1 + \gamma - \beta\cos vt$ where the amplitude β and the offset γ are zero at the equilibrium $x = X = 0$ and slowly grow together with the libration amplitude. So, we are not going to discuss the libration case in details, but the Mathieu-style patterns inside this zone are clearly visible. In Fig. 4, we present two OFLI2 plots for $y = 10^{-5}$ (we will obtain similar pictures with any other indicator using 3D initial variations for the MEGNO and FLI and also slightly perturbed y for the IACF). Fig. 4a shows a parametric dependence of the variational chaos indicator: we fixed $x = 0$ and we change the parameter a vs. the velocity X.

As an additional check, we have generated in Fig. 5 the (a) SN and (b) IACF maps of the variables x and X with the initial condition $y = 10^{-5}$ that confirm the instability in the second degree of freedom.

Thus we can conclude, that the positive MLCE detected by the variational methods are not numerical artifacts, and they had to appear due to the exponential instability of variables y and Y. But the positive MLCE alone is not the evidence of chaos, as we have reminded in Section 2.1: actually there is no contradiction between the spectral methods results that say the motion is periodic or quasi-periodic, and the variational methods that say these (quasi)periodic orbits are exponentially unstable. What we obtain from the two methods is not a paradox but a complementary information.

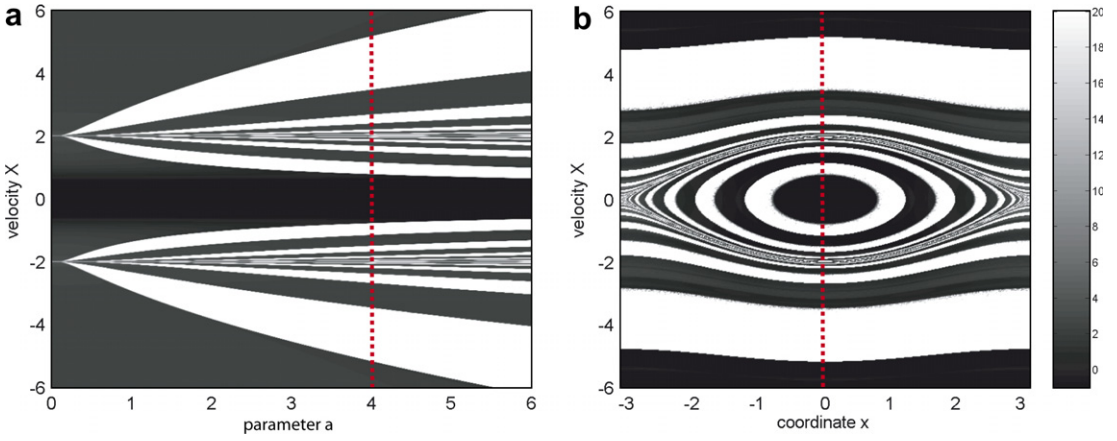

Fig. 4. (a) OFLI2 parametric evolution a vs. the X and (b) OFLI2 x vs. X plot.

Please cite this article in press as: Barrio R et al., Spurious structures in chaos indicators maps, Chaos, Solitons & Fractals (2007), doi:10.1016/j.chaos.2007.09.084

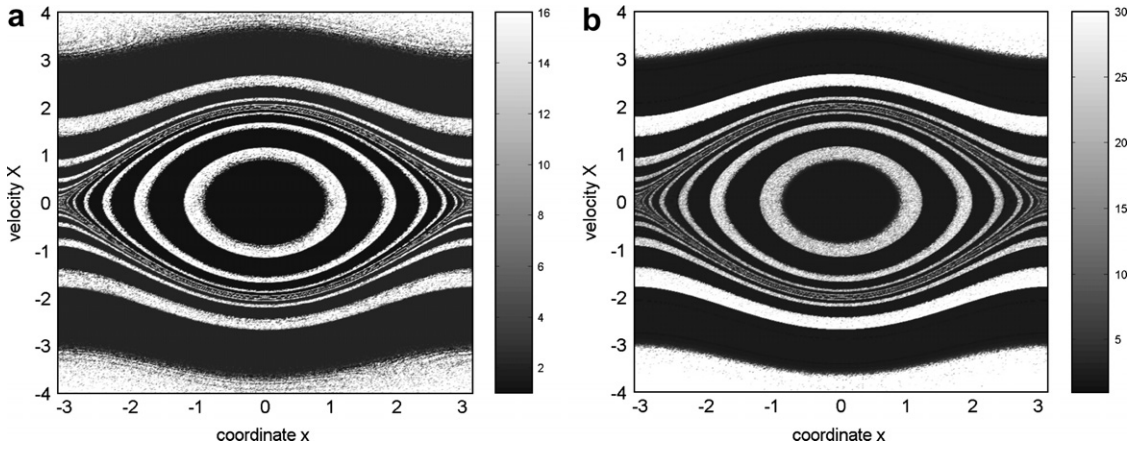

Fig. 5. (a) SN and (b) IACF maps x vs. X with the initial condition $y = 10^{-5}$.

4.2. Back to the plane – variational methods

As we already have mentioned, there are some spurious patterns of low MEGNO and FLI in Fig. 3b and d. What is their origin? In order to answer this question we focus our attention on the 2D pendulum problem where $\boldsymbol{\rho} = (x, X)^{\top}$ and $\boldsymbol{\xi} = (\delta x, \delta X)^{\top}$. In Fig. 6, we show the MEGNO, FLI and OFLI2 plots up to the final time $t_f = 500$. In this first test we use initial conditions of the variational equations $\boldsymbol{\xi}(0) = (1, 1)^{\top}$ for the MEGNO and FLI methods, whereas OFLI2 uses the usual fixed set of initial conditions.

The FLI and MEGNO maps in Fig. 6 clearly present the patterns that were pushed the background in Fig. 3: the sine wave shaped "hyperstable" regions. The existence of these patterns does not influence the general conclusion about the non-chaotic motion of the pendulum, yet they are not welcome, suggesting that the same periodic trajectory is more or less regular depending on the initial conditions choice. Interestingly the OFLI2 results are free from this phenomenon that seems generic for almost any MEGNO and FLI plot (as already mentioned in [16]). If we want to know how to avoid this kind of artifacts we have to understand their origin. Thus the next section is devoted to explaining what is the origin of these "sine waves", will they always look the same and why we do not see them in the OFLI2.

4.2.1. Low MLCE waves: more on Lyapunov exponents

Recalling that variational methods tend to estimate the maximum Lyapunov characteristic exponent, let us first review some results of the Lyapunov exponents theory. In the continuous case, we have a dynamical system [39] on the state space M defined by a diffeomorphic flow map

$$\begin{aligned} \phi^t : \quad & M \to M, \\ & \boldsymbol{\rho} \mapsto \phi^t(\boldsymbol{\rho}) \end{aligned}$$

given by an ordinary differential equation $\dot{\boldsymbol{\rho}} = \boldsymbol{f}(\boldsymbol{\rho})$ with formal solution $\boldsymbol{\rho} = \boldsymbol{\rho}(t; \boldsymbol{\rho}_0) = \phi^t(\boldsymbol{\rho}_0) \in M$. The Lyapunov exponents are based on the solution on the standard orthonormal basis of the linearized flow map Y that maps the tangent space $T_{\boldsymbol{\rho}_0} M$ into $T_{\phi^t(\boldsymbol{\rho}_0)} M$ and is given by the resolvent (or stability matrix) of the matrix linear system

$$\dot{Y}(t) = D\boldsymbol{f}(t, \boldsymbol{\rho}(t)) Y(t) := \frac{\partial \boldsymbol{f}(t, \boldsymbol{\rho}(t))}{\partial \boldsymbol{\rho}} Y(t), \quad Y(0) = \mathbb{Y},$$

where $\mathbb{Y}$ denotes any orthonormal basis (usually we take $\mathbb{Y} = \mathbb{I}$, that is, the identity matrix). Once we have the resolvent we have all the solutions of the variational equations on the form $\boldsymbol{\xi}(t) = Y(t)\boldsymbol{\xi}_0$. The resolvent matrix may have complex eigenvalues, so – in order to simplify the stability analysis – it is common to use the singular value decomposition (SVD) of the resolvent [40]. That is, to put $Y = UDV^{\top}$ with U and V orthogonal matrices and D diagonal. The diagonal elements of D are the square roots of the eigenvalues of the matrix $Y^{\top}Y$, which is now a symmetric positive definite matrix, hence its eigenvalues are real and its eigenvectors form an orthogonal basis. We denote by $\Lambda_i(t; \mathbb{Y})$ the eigenvalues of $Y^{\top}Y$ at time t and using the initial matrix $\mathbb{Y}$.

Please cite this article in press as: Barrio R et al., Spurious structures in chaos indicators maps, Chaos, Solitons & Fractals (2007), doi:10.1016/j.chaos.2007.09.084

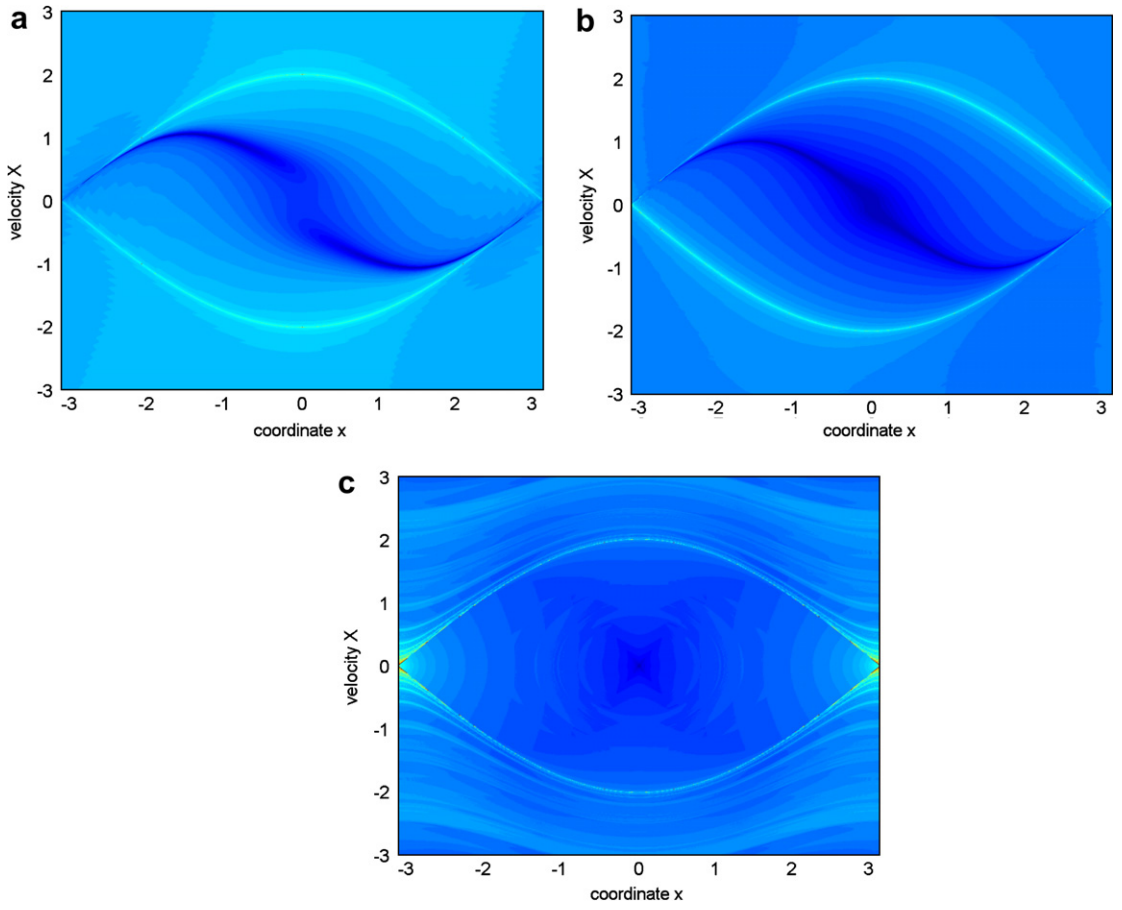

Fig. 6. (a) MEGNO, (b) FLI and (c) OFLI2 plots for the pendulum problem.

Definition 2. *We call* local or finite-time Lyapunov exponents *the real numbers*

$$\lambda_i(t;\mathbb{Y}) := \frac{1}{2t}\ln \Lambda_i(t;\mathbb{Y})$$

and local or finite-time Lyapunov vectors *the eigenvectors of*

$$Y^{\top}(t;\mathbb{Y})Y(t;\mathbb{Y}).$$

The matrix $Y^{\top}Y$ may be also interpreted in a more geometrical setting as the flat metric tensor of Eulerian space transformed to Lagrangian coordinates (for details see [41]).

The asymptotic behavior of the finite-time Lyapunov exponents and vectors is governed by the multiplicative ergodic theorem of Osedelec [42] that states that for any ergodic probability measure p on the state space $M = \mathbb{R}^n$ and for any solution $\boldsymbol{y}(t)$ of the differential equation we have [43]:

(1) For p-almost all $\boldsymbol{v} \in \mathbb{R}^n$, there exists a finite exponent

$$\lambda = \lim_{t\to\infty}\frac{1}{t}\ln\frac{\|Y(t)\boldsymbol{v}\|}{\|\boldsymbol{v}\|},$$

that does not depend on the initial time and takes at most n values $\lambda_1 \geqslant \lambda_2 \geqslant \cdots \geqslant \lambda_n$ (*the Lyapunov exponents*).

(2) There exists the limit matrix

$$L(t_0) = \lim_{t\to\infty}\{Y^{\top}(t;\mathbb{Y})Y(t;\mathbb{Y})\}^{1/2t}.$$

Please cite this article in press as: Barrio R et al., Spurious structures in chaos indicators maps, Chaos, Solitons & Fractals (2007), doi:10.1016/j.chaos.2007.09.084

The non-integer power of the matrix $Y^\top Y$ is defined by diagonalization. Note that this fact asses that the finite-time Lyapunov exponents $\lambda_i(t;\mathbb{Y})$ will have a limit, the Lyapunov exponents λ_i of the orbit.

(3) There exists a sequence of embedded subspaces

$$S_n(t_0) \subset S_{n-1}(t_0) \subset \cdots \subset S_1(t_0) = \mathbb{R}^n,$$

such that on the complement $S_i(t_0) \setminus S_{i+1}(t_0)$ of $S_{i+1}(t_0)$ in $S_i(t_0)$ the exponential growth (or decay) rate is λ_i.

The eigenvectors $\boldsymbol{l}_i$ of the limit matrix $L(t_0)$ are called Lyapunov vectors and the ith one belongs to $S_i(t_0) \setminus S_{i+1}(t_0)$. The convergence of the Lyapunov vectors is exponential, so its behavior at finite-time describes well its asymptotic limit, but the convergence of the Lyapunov exponents is very slow. This fact is usually employed to obtain the MLCE (the kernel of all the variational indicators). However, problems appear when all $\lambda_i = 0$. Now, following the ergodic theorem it is not easy to compute for all the orbits the same Lyapunov exponent (in fact the same finite-time Lyapunov exponent).

The key point to study some spurious patterns is to study the directions associated with zero Lyapunov exponents.

Proposition 3. *The function $V = \boldsymbol{f}(t,\boldsymbol{\rho})$ is the solution of the variational equation (2) with initial conditions $\boldsymbol{\xi}_0 = \boldsymbol{f}(t_0,\boldsymbol{\rho}_0)$. Moreover, if the support of the ergodic measure p does not reduce to a fixed point then these initial conditions in the variational equations generate a zero Lyapunov exponent.*

Proposition 3 [44] establishes that for any orbit at least one Lyapunov exponent vanishes. We may enforce the above result just pointing that the solution of the variational equations using any vector tangent to the flow will generate a solution tangent to the flow with the same proportionality constant.

But, what happens if we work with Hamiltonian systems? Now the differential system and the Lyapunov spectra possess a specific structure [45]. Given a $2n$ degrees of freedom Hamiltonian function $\mathscr{H}$ the differential system is given by

$$\dot{\boldsymbol{\rho}} = J\nabla\mathscr{H}$$

with J the skew-symmetric matrix

$$J = \begin{pmatrix} 0 & \mathbb{I} \\ -\mathbb{I} & 0 \end{pmatrix}.$$

In this case the stability matrix Y is symplectic (that is, $YJY^\top = J$) and, for conservative Hamiltonians, if λ_i is a Lyapunov exponent then also $-\lambda_i$ is another one: the exponents are grouped in pairs. Therefore, as at least one Lyapunov exponent is zero, automatically two of them are zero. Moreover, [46], if $\mathscr{H}$ is constant then for any solution $\boldsymbol{\xi}(t)$ of (2) one has

$$\frac{\mathrm{d}}{\mathrm{d}t}\langle \boldsymbol{\xi}(t), \nabla\mathscr{H}\rangle = 0.$$

An important consequence of the above result is that if a solution of the variational equation is orthogonal to $\nabla\mathscr{H}$ at any time, then it will always remain orthogonal. Also, the projection of $\boldsymbol{\xi}(t)$ onto such a vector is constant. Besides, the vector $\nabla\mathscr{H}$ is a Lyapunov vector associated with a zero Lyapunov exponent [46]. In fact, any given conserved quantity gives two zero Lyapunov exponents. Also, by Noether's theorem, a symmetry in the dynamics implies a zero Lyapunov exponent. A completely different behavior is associated to the projection onto the tangential direction of the flow: no answer can be given for $\langle \boldsymbol{\xi}(t), \boldsymbol{f}(t,\boldsymbol{\rho})\rangle = \langle \boldsymbol{\xi}(t), J\nabla\mathscr{H}\rangle$. So, even the first Lyapunov vector cannot be made orthogonal to the flow at every instant.

These two special directions $J\nabla\mathscr{H}$ and $\nabla\mathscr{H}$ are usually considered as marginal. The displacement in the direction of $J\nabla\mathscr{H}$ gives just a displacement in the reference trajectory and the displacement in the direction of $\nabla\mathscr{H}$ will give rise to a transfer to a nearby orbit with a Hamiltonian value different from that of the reference one. Therefore, several strategies have been designed to separate these Lyapunov vectors from the rest [46] (in [47] a special algorithm is designed to maintain these vectors for dissipative systems). But what happens if all the Lyapunov exponents vanish as it happens for regular orbits? This is precisely the situation where the chaos indicators based on first-order variational equations seem to have problems and generate spurious patterns. So, a priori, methods based on second- (or higher) order variational equations (OFLI2) are more suitable when all the Lyapunov exponents vanish.

In conservative Hamiltonians with one degree of freedom the situation is quite simple: for each orbit both Lyapunov exponents vanish. The direction tangent to the flow generates a very low value of the variational chaos indicators because for periodic orbits the ratio $\|\boldsymbol{f}(t)\|/\|\boldsymbol{f}(t_0)\|$ has only small variations. Thus we may expect that if the initial conditions of the variational equations follow that direction only for some orbits, then we will obtain spurious patterns. Let us return to Fig. 6. The methods that use first-order variational equations (MEGNO and FLI) exhibit a spurious line. In order to have an initial vector $\boldsymbol{\xi}_0 = (\delta x_0, \delta y_0)^\top$ for the variational equations tangent to the flow in the pendulum equations

Please cite this article in press as: Barrio R et al., Spurious structures in chaos indicators maps, Chaos, Solitons & Fractals (2007), doi:10.1016/j.chaos.2007.09.084

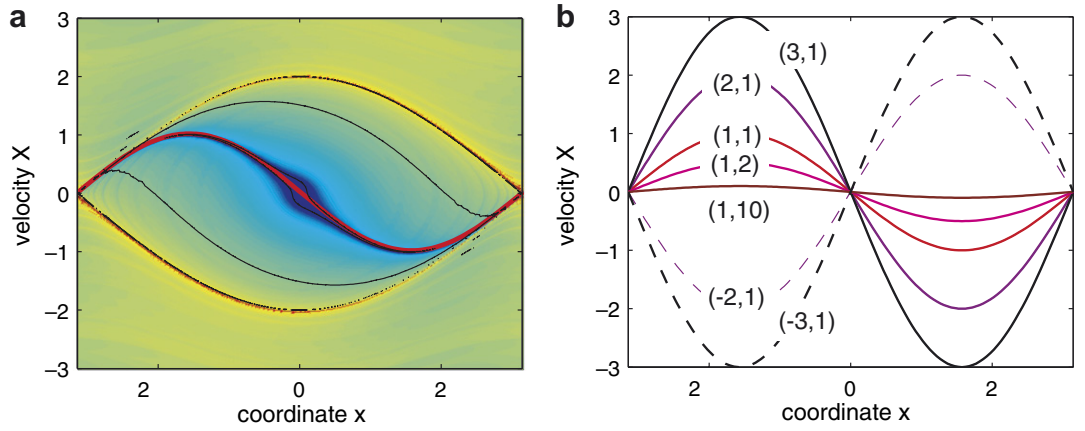

Fig. 7. (a) FLI plot of Fig. 6, its contour plot and (in red) the theoretical predicted spurious pattern and (b) theoretical predicted spurious patterns for several choices of the initial conditions of the variational equations.

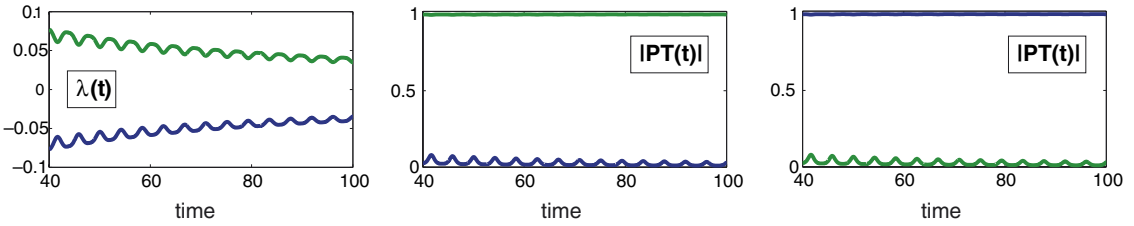

Fig. 8. Finite-time Lyapunov exponents ($\lambda(t)$) and normalized projections of the finite-time Lyapunov vectors onto the tangent of the flow $|\mathrm{PT}(t)|$ and onto the gradient of the Hamiltonian (the normal direction) $|\mathrm{PN}(t)|$.

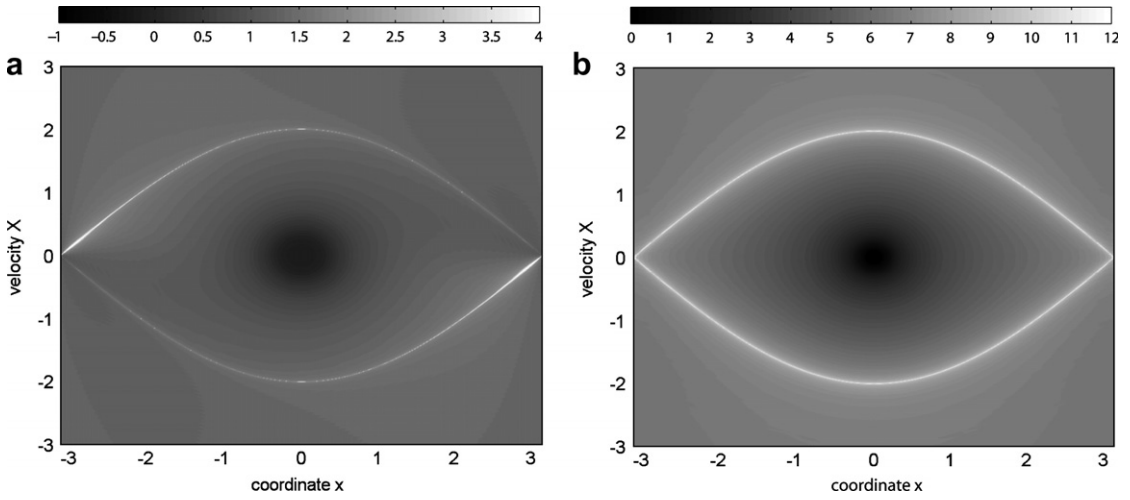

Fig. 9. (a) MEGNO and (b) FLI plots for the pendulum problem using the gradient to the Hamiltonian as initial conditions.

Please cite this article in press as: Barrio R et al., Spurious structures in chaos indicators maps, Chaos, Solitons & Fractals (2007), doi:10.1016/j.chaos.2007.09.084

$$\dot{x} = y, \quad \dot{y} = -\sin x,$$

we need

$$y_0\,\delta y_0 = -\sin(x_0)\delta x_0.$$

And so, for $\delta y_0 \neq 0$

$$y_0 = -\frac{\delta x_0}{\delta y_0}\sin(x_0).$$

In Fig. 7a, we show (in red on the web) the curve of points where the initial variation vector $(1,1)^{\top}$ is tangent to the flow. This figure coincides quite well with the observed spurious patterns in Fig. 6. Fig. 7b presents the theoretical pre-

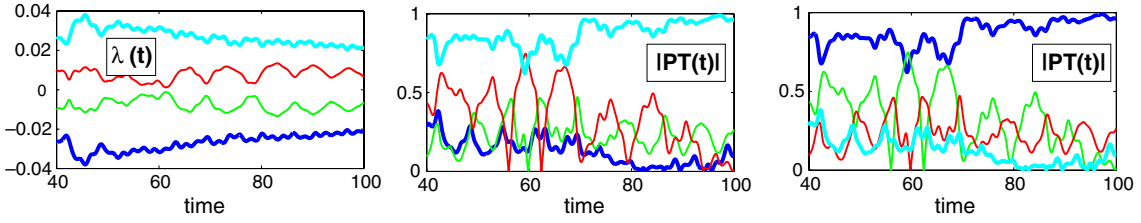

Fig. 10. Finite-time Lyapunov exponents ($\lambda(t)$) and normalized projections of the finite-time Lyapunov vectors onto the tangent of the flow $|\mathrm{PT}(t)|$ and onto the gradient of the Hamiltonian $|\mathrm{PN}(t)|$ for the Hénon–Heiles problem.

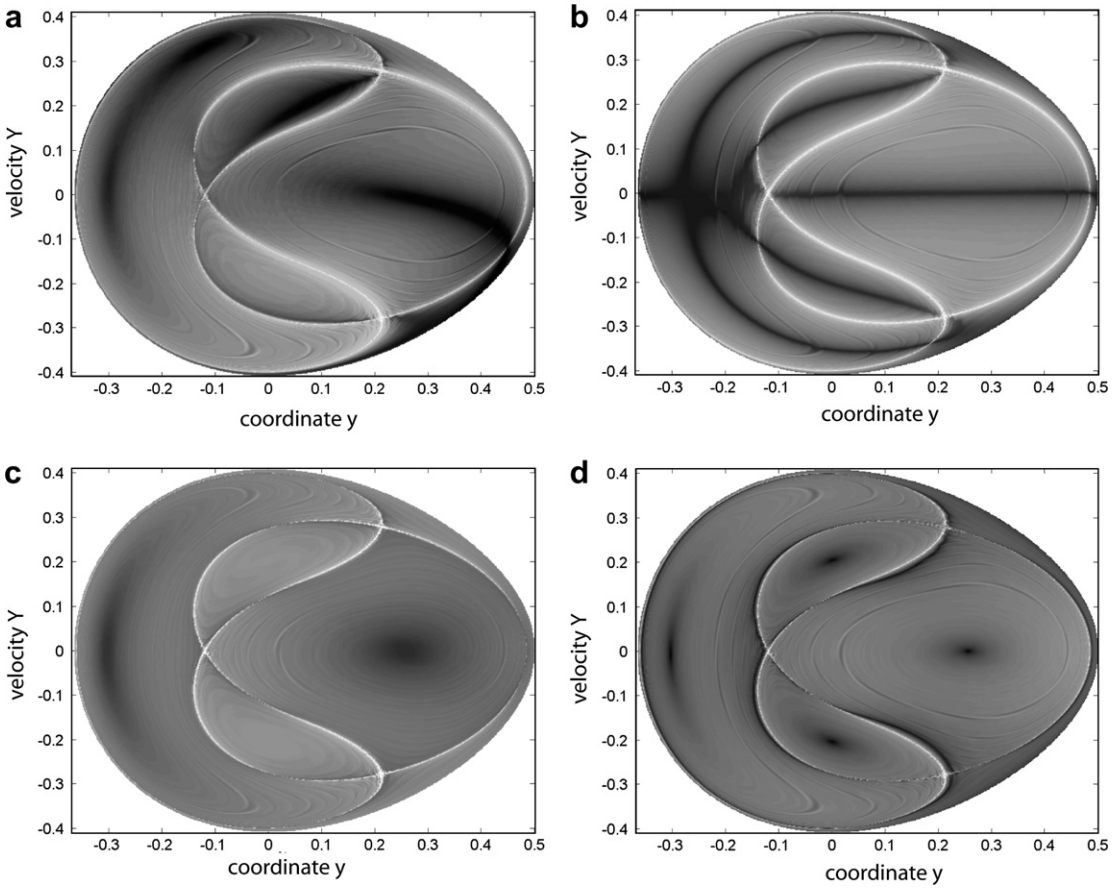

Fig. 11. (a) "Bad" FLI plot (with initial conditions for the variational equation $(1,-1,1,1)/2$), (b) "Bad" FLI plot (with initial conditions for the variational equation $(-f_4,-f_3,f_2,f_1)/\|\boldsymbol{f}\|$), (c) "Good" FLI plot (initial vector $-\nabla\mathscr{H}/\|\nabla\mathscr{H}\|$) and (d) OFLI2 plot.

Please cite this article in press as: Barrio R et al., Spurious structures in chaos indicators maps, Chaos, Solitons & Fractals (2007), doi:10.1016/j.chaos.2007.09.084

diction of the spurious patterns for several choices of the initial vector for the variational equations. Experimenting with various ξ_0 we have recovered the same patterns in MEGNO and FLI maps for the pendulum.

According to the above discussion, it seems reasonable to avoid the tangent direction when we use first-order variational equations. In Hamiltonians with just one degree of freedom there is actually a single choice to avoid the tangent: the vector orthogonal to the flow, that in this case coincides with the gradient of the Hamiltonian $\nabla\mathscr{H}$. Then the vector ξ evolving in time always has an orthogonal component although a tangent one will also appear. This fact prevent us from approaching the Lyapunov vector as fast as we would like. In Fig. 8 we show, for the orbit with initial conditions $(x, y) = (-2, 0.1)$, the finite-time Lyapunov exponents and the normalized projections of the updated finite-time Lyapunov vectors onto the tangent of the flow and onto $\nabla\mathscr{H}(t)$. Both finite-time Lyapunov exponents converge to zero and the finite-time vectors converge to the tangent to the flow and to the gradient vector.

Let us see how this strategy works in the pendulum problem. We compute the MEGNO and FLI indicators using initial vectors $\nabla\mathscr{H}/\|\nabla\mathscr{H}\|$. The results shown in Fig. 9 suggest that now the FLI indicator works quite well and also the MEGNO one (although it seems that MEGNO needs more integration time in order to correct some rotations).

Let us now consider a Hamiltonian system with more degrees of freedom. In order to compare with quite well known results [48] we just show a brief comparison for the Hénon–Heiles problem with energy $E = 1/12$. Fig. 9 presents the finite-time Lyapunov exponents and normalized projections of the updated finite-time Lyapunov vectors onto the tangent of the flow and onto $\nabla\mathscr{H}(t)$, obtained for the orbit with initial conditions $(x, y, Y) = (0, -0.2, 0.2)$ and X computed from the energy integral. All the finite-time Lyapunov exponents converge to zero, and one Lyapunov vectors converges to the tangent to the flow and another one to the gradient vector (see Fig. 10).

Using the FLI map as an example, we present the results of various ξ choice strategies in Fig. 11. The first FLI plot (Fig. 11a) was obtained using a fixed initial variation vector, whereas the second (Fig. 11b) and the third (Fig. 11c) were generated using two different vectors orthogonal to the tangent (the case (c) uses the marginal direction given by the gradient of the Hamiltonian). One can observe that the best FLI map was obtained in the case (c), that is, using the

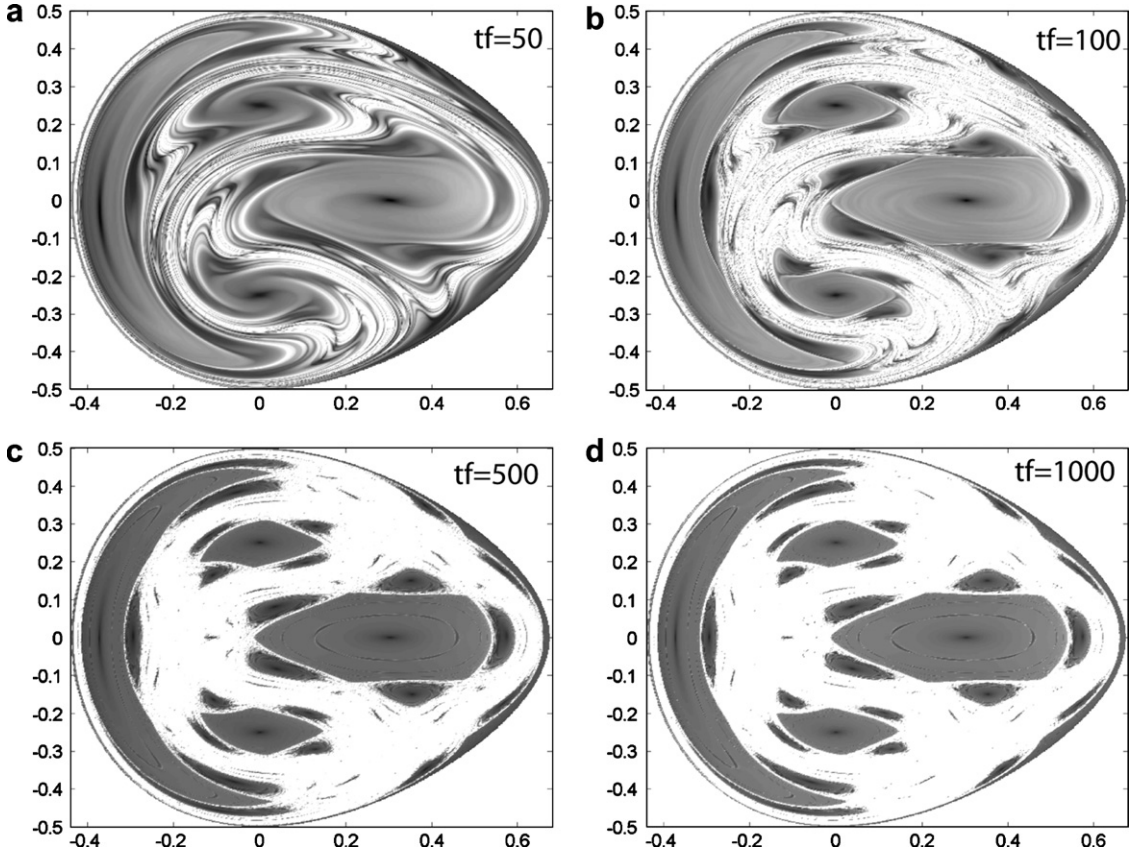

Fig. 12. OFLI2 plots of the Hénon–Heiles system with energy $E = 1/8$ using different final times $t_f = 50$, 100, 500 and 1000.

Please cite this article in press as: Barrio R et al., Spurious structures in chaos indicators maps, Chaos, Solitons & Fractals (2007), doi:10.1016/j.chaos.2007.09.084

same direction of ξ that worked best in the analysis of the 2D pendulum problem. The fourth map (Fig. 11d) is an OFLI2 plot and we observe that this indicator did not produce any remarkable spurious pattern. Therefore, it seems that the choice of ξ in the direction of $\pm\nabla\mathscr{H}$ permits to reduce significantly the spurious structures in first-order variational chaos indicators.

Before closing this section, we have to mention another way of getting rid of spurious patterns that amounts to a random selection of ξ_0 [22]. Leaving apart the fact that it results in a noisy map of chaos indicator, we have to warn that manipulating the units of length and time, one may create some preferred directions of ξ_0 and simple random draw of variations components may become practically similar to the constant ξ_0 selection. An appropriate modification of the random choice procedure can be found in [19].

4.3. The significance of integration time

After the discussion of spurious structures of the variational methods due to the initial conditions of the variational equations, let us mention another sources of artifacts: the final time of simulations. If the final time is too large we may have two problems, the first one is just the total computing time (in some case prohibitive) and the second one are the precisions problems due to the rounding errors. On the contrary, a too short final time may result in a completely wrong dynamical picture.

In Fig. 12, we present some OFLI2 plots[4] for the Hénon–Heiles system. The pictures have been obtained on the y vs. Y plane for $x = 0$ and X obtained from the constant value of the energy $E = 1/8$. We have used four different final times $t_f = 50$, 100, 500 and 1000. From the first two pictures we may infer completely wrong results, especially with the first one that in fact is not symmetric in spite of the symmetry of the problem. Thus a correct selection of the final time is essential, but how to choose a correct one? Well, this is the key point and there is no complete answer for any method in the literature. One ''rule of thumb'' given in [16] is just to start with preliminary simulations (with few initial points) until the final picture do not change significantly (like Fig. 12c and d); then, knowing the proper integration time, one can compute the definitive map with a large number of initial points.

5. Conclusions

In this paper, we have studied several chaos indicators. We have shown some of typical spurious patterns in stability maps of simple (hence easily comprehensible) systems; the patterns that according to our experience are generic for a wide variety of problems. The most important recommendation that we suggest is not to rely on a single type of indicator. Confronting the results of a variational method and of a spectral method well protects against taking an unstable regular orbit for a chaotic one, or contrarily – it does not let the instability of a regular orbit to pass unnoticed. Although we demonstrated this phenomenon on a simple, ad hoc test problem, we met it in a more intricate study of spin–orbit coupling between a sphere and an ellipsoid [19]; interestingly, the Poincaré section for the Saturn satellite Hyperion so often reproduced in literature is to some extent misleading: it presents the planar case, taking no account for the instability in the neglected degree of freedom – exactly the same way as the pendulum case discussed in this paper.

Noticing that both kinds of methods have different types of spurious patterns, comparing the two maps of chaos indicators one can easily tell essential features from accidental ones. Nevertheless, all indicators should be used in a way that inhibits the occurrence of artifacts. On one hand, a sufficiently long time interval should be used, according to some preliminary tests, in order to avoid incorrect conclusions; on the other hand, a wise choice of initial variation vectors for the first-order variational methods permits to reduce considerably the spurious patterns. In this paper we have pointed out one ''good'' initial vector for Hamiltonian problems. The spectral methods and the OFLI2 method, based on second-order variational equations, seem to be more robust with respect to the generation of spurious patterns.

References

[1] Devaney RL. An introduction to chaotic dynamical systems. Studies in nonlinearity. Boulder (CO): Westview Press; 2003. Reprint of the second (1989) edition.

[4] For any other variational method the conclusions are similar. For example, the MEGNO plots look so similar that we do not reproduce them.

Please cite this article in press as: Barrio R et al., Spurious structures in chaos indicators maps, Chaos, Solitons & Fractals (2007), doi:10.1016/j.chaos.2007.09.084

[2] Banks J, Brooks J, Cairns G, Davis G, Stacey P. On Devaney's definition of chaos. Am Math Mon 1992;99(4):332–4.
[3] Awrejcewicz J, Dzyubak L, Grebogi C. A direct numerical method for quantifying regular and chaotic orbits. Chaos, Solitons & Fractals 2004;19:503–7.
[4] Bashkirtseva I, Ryashko L. Sensitivity and chaos control for the forced nonlinear oscillations. Chaos, Solitons & Fractals 2005;26(5):1437–51.
[5] Buszko K, Stefánski K. Measuring transient chaos in nonlinear one- and two-dimensional maps. Chaos, Solitons & Fractals 2006;27(3):630–46.
[6] Li C. A new method of determining chaos-parameter-region for the tent map. Chaos, Solitons & Fractals 2004;21(4):863–7.
[7] Furui S. An analysis of chaos via contact transformation. Chaos, Solitons & Fractals 2004;19(4):743–57.
[8] Szydłowski M. Chaos and time coordinate. Chaos, Solitons & Fractals 1996;7(5):681–95.
[9] Eckmann JP, Ruelle D. Ergodic theory of chaos and strange attractors. Rev Mod Phys 1985;57:617–56.
[10] Schuster HG. Deterministic chaos. An introduction. Weinheim: VCH; 1988.
[11] Lichtenberg AJ, Lieberman MA. Regular and chaotic dynamics. New York: Springer-Verlag; 1992.
[12] Alligood KT, Sauer TD, Yorke JA. Chaos – an introduction to dynamical systems. New York: Springer-Verlag; 1996.
[13] Cincotta PM, Simó C. Simple tools to study global dynamics in non-axisymmetric galactic potentials – I. Astron Astrophys Suppl 2000;147:205–28.
[14] Fouchard M, Lega E, Froeschlé C, Froeschlé C. On the relationship between fast Lyapunov indicator and periodic orbits for continuous flows. Celestial Mech Dyn Astron 2002;83(1–4):205–22.
[15] Froeschlé C, Lega E. On the structure of symplectic mappings. The fast Lyapunov indicator: a very sensitivity tool. Celestial Mech Dyn Astron 2000;78:167–95.
[16] Barrio R. Sensitivity tools vs. Poincaré sections. Chaos, Solitons & Fractals 2005;25(3):711–26.
[17] Barrio R. Painting chaos: a gallery of sensitivity plots of classical problems. Int J Bifurcat Chaos 2006;16(10):2777–98.
[18] Cincotta PM, Giordano CM, Simó C. Phase space structure of multi-dimensional systems by means of the mean exponential growth factor of nearby orbits. Physica D 2003;182:151–78.
[19] Breiter S, Melendo B, Bartczak P, Wytrzyszczak I. Synchronous motion in the Kinoshita problem. Application to satellites and binary asteroids. Astron Astrophys 2005;437:753–64.
[20] Breiter S, Wytrzyszczak I, Melendo B. Long-term predictability of orbits around the geosynchronous altitude. Adv Space Res 2005;35:1313–7.
[21] Goździewski K. Stability of the HD 12661 planetary system. Astron Astrophys 2003;398:1151–61.
[22] Goździewski K, Bois E, Maciejewski AJ, Kiseleva-Eggleton L. Global dynamics of planetary systems with the MEGNO criterion. Astron Astrophys 2001;378:569–86.
[23] Pavlov AI, Maciejewski AJ. An efficient method for studying the stability and dynamics of the rotational motions of celestial bodies. Astron Lett 2003;29:552–66.
[24] Pérez MJ, Cincotta PM, Giordano CM. Global dynamics in elliptical galaxies. In: Revista Mexicana de Astronomía y Astrofísica conference series, 2003. p. 187.
[25] Barrio R, Blesa F, Serrano S. Qualitative analysis of the $(N+1)$-body ring problem. Chaos, Solitons & Fractals 2006. doi:10.1016/j.chaos.2006.08.007.
[26] Laskar J. The chaotic motion of the solar system – a numerical estimate of the size of the chaotic zones. Icarus 1990;88:266–91.
[27] Laskar J, Froeschlé C, Celletti A. The measure of chaos by the numerical analysis of the fundamental frequencies. Application to the standard mapping. Physica D 1992;56:253–69.
[28] Michtchenko TA, Ferraz-Mello S. Resonant structure of the outer solar system in the neighborhood of the planets. Astron J 2001;122:474–81.
[29] Press WH. Numerical recipes in Fortran 77: the art of scientific computing. Cambridge: Cambridge University Press; 2003.
[30] Sprott JC. Chaos and time-series analysis. Oxford: Oxford University Press; 2003.
[31] Veldman DJ. Fortran programing for the behavioral sciences. New York: Holt, Rinehart and Winston; 1967.
[32] Wahl M, Gregor I, Patting M, Enderlein J. Fast calculation of fluorescence correlation data with asynchronous time-correlated single-photon counting. Opt Express 2003;11:3583–91.
[33] Barrio R. Sensitivity analysis of ODEs/DAEs using the Taylor series method. SIAM J Sci Comput 2006;27(6):1929–47.
[34] Barrio R, Blesa F, Lara M. VSVO formulation of the Taylor method for the numerical solution of ODEs. Comput Math Appl 2005;50(1–2):93–111.
[35] Yoshida H. Construction of higher order symplectic integrators. Phys Lett A 1990;150:262–8.
[36] Hénon M, Heiles C. The applicability of the third integral of motion: some numerical experiments. Astron J 1964;69:73–9.
[37] Amidror I. The theory of the Moiré phenomenon. Dordrecht: Kluwer; 2000.
[38] Arnold VI. Mathematical methods of classical mechanics. New York: Springer-Verlag; 1997.
[39] Geist K, Parlitz U, Lauterborn W. Comparison of different methods for computing Lyapunov exponents. Progr Theor Phys 1990;83(5):875–93.
[40] Dieci L, Van Vleck ES. Lyapunov and other spectra: a survey. In: Collected lectures on the preservation of stability under discretization (Fort Collins, CO, 2001). Philadelphia (PA): SIAM; 2002. p. 197–218.
[41] Thiffeault J-L, Boozer AH. Geometrical constraints on finite-time Lyapunov exponents in two and three dimensions. Chaos 2001;11(1):16–28.

Please cite this article in press as: Barrio R et al., Spurious structures in chaos indicators maps, Chaos, Solitons & Fractals (2007), doi:10.1016/j.chaos.2007.09.084

[42] Osedelec VI. A multiplicative Ergodoc theorem. Lyapunov characteristic numbers for dynamical systems. Trans Moscow Math Soc 1968;19:197–231.
[43] Legras B, Vautard R. A guide to Lyapunov vectors. in: Palmer T, editor. Predictability (vol. I), ECWF Seminar, ECMWF, Reading, UK, 1996. p. 135–46.
[44] Haken H. At least one Lyapunov exponent vanishes if the trajectory of an attractor does not contain a fixed point. Phys Lett A 1983;94(2):71–2.
[45] Meyer HD. Theory of the Lyapunov exponents of hamiltonian systems and a numerical study on the transition from regular to irregular classical motion. J Chem Phys 1986;84:3147–61.
[46] Yamaguchi YY, Iwai T. Geometric approach to Lyapunov analysis in Hamiltonian dynamics. Phys Rev E 2001;64 (6, part 2)(3):066206. 16.
[47] Grond F, Diebner HH, Sahle S, Mathias A, Fischer S, Rossler OE. A robust, locally interpretable algorithm for Lyapunov exponents. Chaos, Solitons & Fractals 2003;16(5):841–52.
[48] Benettin G, Galgani L, Strelcyn JM. Kolmogorov entropy and numerical experiments. Phys Rev A 1976;14:2338–45.

Please cite this article in press as: Barrio R et al., Spurious structures in chaos indicators maps, Chaos, Solitons & Fractals (2007), doi:10.1016/j.chaos.2007.09.084